Structure and Surface Properties of Size-tuneable $CsPbBr_3$ Nanocrystals

Received 00th January 20xx,
Accepted 00th January 20xx

DOI: 10.1039/x0xx00000x

Thomas J. N. Hooper,*[a] Fang Yanan,[b] Alasdair A. M. Brown,[c,d,e,] Suan Hui Pu,[c,d] Tim J. White*[b,e]

This investigation has characterised the structure and surface chemistry of $CsPbBr_3$ nanocrystals with controlled diameters between 6.4 to 12.8 nm. The nanocrystals were investigated via a thorough ^{133}Cs solid state NMR and nuclear relaxation study, identifying and mapping radially-increasing nanoscale disorder. This work has formalised ^{133}Cs NMR as a highly sensitive probe of nanocrystal size, which can conveniently analyse nanocrystals in solid forms, as they would be utilised in optoelectronic devices. A combined multinuclear solid state NMR and XPS approach, including ^{133}Cs-^{1}H heteronuclear correlation 2D (HETCOR) NMR, was utilised to study the nanocrystal surface and ligands, demonstrating that the surface is Cs-Br rich with vacancies passivated by didodecyldimethylammonium bromide (DDAB) ligands. Furthermore, it is shown that a negligible amount of phosphonate ligands remain on the powder nanocrystal surface, despite the key role of octylphosphonic acid (OPA) in controlling the colloidal nanocrystal growth. The $CsPbBr_3$ NCs were shown to be structurally stable under ambient conditions for up to 6 months, albeit with some particle agglomeration.

Introduction

Cesium lead halide perovskite nanocrystals (NCs) have been established as one of the most promising materials for light-emitting applications. They have exhibited near-unity photoluminescence quantum yields (PLQY) and extremely narrow emission bandwidths (FWHM < 20 nm).[1–6] The all-inorganic nature of $CsPbX_3$ nanocrystals provides greater thermal, environmental and light stability, which has been a hindrance to its organic-inorganic hybrid counterparts.[7–9] The structural lability of the perovskite lattice enables exchange of the halide anions, even post-synthetically, to adjust emission energy over the entire visible spectrum.[10,11] The size of the nanocrystals afford a further mechanism to control the emission wavelength. Light emitting NCs with dimensions smaller than their exciton Bohr radii (5 – 12 nm in $CsPbX_3$) benefit from quantum confinement effects, resulting in higher energy emission in smaller nanocrystals.**[11,12]** Hence, the facile colloidal synthesis of $CsPbX_3$ NCs is a great benefit and accurate size control of these NCs is an important area of research.[13] Our recent work demonstrated a room-temperature colloidal synthesis of $CsPbBr_3$ NCs, with photoluminescence quantum yields (PLQYs) above 80 % and fine size-tuneability, enabling the adjustment of the diameter from 6.6 to 13 nm, corresponding to emission wavelengths from 501 to 517 nm.**[12]**

Studies of emerging semiconductor nanocrystals have generally analysed functionality through a focus on synthesis routes, optical properties and colloid stability. While these important considerations dictate whether the materials are intrinsically suitable for light emission technology, the property-determining chemical and structural characteristics are often underexplored. Due to the clear importance of the composition and size of $CsPbX_3$ nanocrystals, their structural characterisation is particularly crucial. Recently, the use of nuclear magnetic resonance (NMR) has become commonplace for this characterisation.[14] Popular solution NMR nuclei, such as ^{1}H, ^{13}C, and ^{31}P NMR, have long been used to reveal the composition and conformation of bound organic ligands in perovskite NC colloids, to help reveal the nature of the ligand binding to the nanocrystal surface.[15–18] Solid state NMR (SSNMR) has also proved useful for NC ligand study, as by analysing the solid nanoparticle precipitate, rather than the colloidal solution, we can ensure that the observed ligand species are attached to the nanocrystal surfaces.[15,19–22]

Additionally, due to its element specific, short-range nature, SSNMR can provide great insight into the local structure of disordered systems such as nanomaterials. This explains the developing interest in SSNMR of perovskite nanocrystals using the perovskite nuclei ^{133}Cs and ^{207}Pb, whose extensive chemical shift ranges can be highly sensitive to different atomic coordination and bonding.[14,23–26] Both techniques have been utilised previously to examine mixed cation and mixed halide perovskites, confirming the monophasic nature of these microcrystalline (bulk) materials.[26–32] Since NMR observes the entirety of a sample, in nanoparticles where the surface-atoms to bulk-atoms ratio is high, it can also reveal properties of the surface chemistry.[20–22,27,33,34] These surface details have been recently observed in ^{133}Cs SSNMR studies of perovskite nanocrystals but the findings have not yet been fully investigated.

This paper follows on from our previous work on a range of variable sized $CsPbBr_3$ NCs,[12] but investigates the particles in solid state powder form, rather than as NC colloids, providing more relevant results for their application in optoelectronic devices. For the first time an in-depth ^{133}Cs solid state NMR investigation of the NC structure was employed, with an aim to formalise ^{133}Cs NMR as a highly sensitive probe of perovskite NC surface environments and NC particle sizes. The results are

---

[a] *High Field NMR Facility, Division of Physics and Applied Physics, School of Physical and Mathematical Sciences, Nanyang Technological University, 21 Nanyang Link, Singapore 637371, Republic of Singapore*
[b] *School of Materials Science and Engineering, Nanyang Technological University, 50 Nanyang Drive, Singapore, 637553, Republic of Singapore*
[c] *Faculty of Engineering and Physical Sciences, University of Southampton, University Road, Southampton, SO171BJ, United Kingdom*
[d] *University of Southampton Malaysia, Iskandar Puteri, 79200, Johor, Malaysia*
[e] *Energy Research Institute at NTU (ERI@N), Research Techno Plaza, Nanyang Technological University, 50 Nanyang Drive, Singapore, 637553, Republic of Singapore*

† Footnotes relating to the title and/or authors should appear here.

Electronic Supplementary Information (ESI) available: [details of any supplementary information available should be included here]. See DOI: 10.1039/x0xx00000x

married with a multinuclear (^{13}C, ^{31}P and ^{133}Cs-^{1}H HETCOR) SSNMR and x-ray photoelectron spectroscopy (XPS) study of the NC surface and ligands.

Experimental

Synthesis

Lead bromide ($PbBr_2$, 99.99 %), cesium bromide (CsBr, 99%), cesium carbonate (Cs_2CO_3, >99.9 %), dimethyl sulfoxide (DMSO, 99%), octanoic acid (OctAc, 98 %), trioctylphosphine oxide (TOPO, 99 %), didodecyldimethylammonium bromide (DDAB, 98 %), ethyl acetate (EtOAc, anhydrous, >99.9 %), methyl acetate (MeOAc, anhydrous, >99.9 %), toluene (anhydrous, >99.8 %) and heptane (anhydrous, 99 %) were purchased from Sigma-Aldrich. Octylphosphonic acid (OPA, 98 %) was purchased from TCI. All chemicals were used without further purification.

To produce the bulk $CsPbBr_3$ sample a 1 M solution of CsBr and $PbBr_2$ in DMSO (0.5 mL), prepared under N_2, was added to toluene (10 mL) under vigorous stirring. Centrifugation produced the precipitate which was dried under vacuum line.

The $CsPbBr_3$ NC precursors were produced as follows: Cs_2CO_3 (32.6 mg, 0.1 mmol) was dissolved in OctAc (1 mL) with stirring at room temperature to form a Cs-octanoate solution; $PbBr_2$ (550 mg, 1.5 mmol) was dissolved in toluene (10 mL), by adding TOPO (5.8 g, 6.44 mL, 15 mmol) and heating at 80 °C for 15 minutes; OPA (0.1 – 0.4 M) was added to the lead halide precursor solution and dissolved with stirring; and DDAB (23.2 mg, 0.05 mmol) was dissolved in toluene (1 mL). To synthesize the $CsPbBr_3$ nanocrystals, 55 μL Cs-octanoate solution was injected into a 0.5 mL PbBr2 solution at room temperature (approx. 25 °C) with vigorous stirring. After 30 to 600 s, 156 μL DDAB solution was added. After a further 300 s, the precipitate was collected by centrifugation with 1.5 mL ethyl acetate at 10000 rpm and redispersed in 100 μL heptane. The dispersion was centrifuged at 5000 rpm and the precipitate discarded. The supernatant was retained and 300 μL methyl acetate was added to fully precipitate the nanocrystals. The precipitate was collected by centrifugation at 10000 rpm and redispersed in 100 μL heptane. Another 300 μL methyl acetate was added to fully precipitate the nanocrystals again, followed by centrifugation at 10000 rpm and redispersion in 100 μL heptane. The dispersion was centrifuged at 5000 rpm and the supernatant was extracted as the fully-purified $CsPbBr_3$ nanocrystal ink. Powder nanocrystal samples were produced via drying the colloids in air for 15 mins. Selected nanocrystal samples were aged for 6 months in ambient conditions to investigate sample degradation.

Analytical methods

The SAXS data were recorded by a Xenocs Nano-inXider equipped with a Dectris Pilatus 3 hybrid pixel detector. The samples were measured in sealed glass capillaries at room temperature. Particle size distributions were obtained from scattering curves using the Monte Carlo-based software package McSAS.

TEM experiments were performed on a JEOL 2100F TEM with a field-emission gun operating at 200 kV. The nanoparticles were deposited on a holey carbon-coated copper grid by submerging the grid in a diluted nanocrystal dispersion followed by air drying.

Powder X-ray diffraction patterns were collected with a Bruker D8 Advance diffractometer equipped with a Cu Kα X-ray tube operating at 40 kV and 40 mA. The experiments were carried at room temperature in air. Rietveld refinements of collected XRD data was performed with TOPAS 3 software.

Solid-state NMR experiments were completed on a 14.1 T Bruker Advance III HD 600 MHz spectrometer. All spectra were processed using the Topspin software package and referenced to the unified scale using IUPAC recommended frequency ratios relative to the ^{13}C adamantane$_{(s)}$ methylene resonance (δ = 37.77 ppm).[35,36] Spectral deconvolution was performed with dmfit.[37] The ^{133}Cs NMR ($\nu_0(^{133}Cs)$ = 78.724 MHz) one-pulse experiments were acquired using a 1.9mm Bruker HXY probe at an MAS frequency of 24 kHz, utilising a non-selective $^{\pi}/_{2}$ pulse of 6.5 μs (determined on $CsCl_{(s)}$) and a recycle delay 5 times the sample's largest measured T_1 to ensure quantitative spectra. The ^{133}Cs spin-lattice relaxation times, T_1, were measured using saturation recovery pulse sequences with a 200 $^{\pi}/_{2}$ pulse saturation block. The ^{207}Pb NMR ($\nu_0(^{207}Pb)$ = 125.60 MHz) experiment was acquired using a 1.9mm Bruker HXY probe at an MAS frequency of 24 kHz. It employed Hahn-echo pulse sequences utilising $^{\pi}/_{2}$ and π pulses of 4.125 and 8.25 μs (determined on $Pb(NO_3)_{2(s)}$), a recycle delay of 10 s, and a rotor synchronised echo delay of 35.48 μs. The ^{1}H NMR one-pulse experiment was acquired using a 4mm Bruker HXY probe at an MAS frequency of 14 kHz, utilising a $^{\pi}/_{2}$ pulse 2.7 μs (determined on adamantane$_{(s)}$) and a recycle delay of 4 s. The ^{13}C[^{1}H] NMR CP experiment was acquired using a 4mm Bruker HXY probe at an MAS frequency of 12 kHz, utilising a 6000 μs contact pulse

Table 1: The synthesis details, peak photoluminescence wavelengths and particle diameters of each of the synthesized $CsPbBr_3$ nanoparticles.

Sample	OPA concentration *(M)*	Reaction duration *(s)*	PL peak wavelength *(nm)*	Mean particle diameter[a] *(nm)*
NC12.8	0.1	600	516 ± 2	12.8 ± 1.0
NC10.4	0.1	300	515 ± 2	10.4 ± 0.9
NC9.9	0.15	300	514 ± 2	9.9 ± 0.8
NC8.9	0.3	300	510 ± 2	8.9 ± 0.6
NC8.3	0.4	300	509 ± 2	8.3 ± 0.5
NC7.7	0.15	120	507 ± 2	7.7 ± 0.4
NC6.4	0.3	30	499 ± 3	6.4 ± 0.5

[a] Determined via Gaussian fitting of particle diameter histograms produced via SAXS analysis of the colloidal solutions.

length, a ^{1}H $^{\pi}/_{2}$ pulse 2.7 μs, high power proton decoupling and a recycle delay of 4 s. The ^{31}P NMR decoupled one-pulse experiment was acquired using a 4mm Bruker HXY probe at an MAS frequency of 14 kHz, utilising a $^{\pi}/_{2}$ pulse 3.8 μs (determined on $(NH_4)H_2PO_{4(s)}$), high power proton decoupling and a recycle delay of 180 s. The ^{133}Cs-^{1}H CPHETCOR NMR experiment was acquired using a 4mm Bruker HXY probe at an MAS frequency of 14 kHz, utilising a 4500 μs contact pulse length, a ^{1}H $^{\pi}/_{2}$ pulse 2.7 μs, high power proton decoupling and a recycle delay of 4 s.

X-ray photoelectron spectroscopy (XPS) analysis was performed using a Kratos AXIS Supra spectrometer with a monochromatic Al Kα source (15 mA, 15 kV). The XPS spectra were collected with solid powder samples pressed on carbon tape. A 3.1-volt bias was applied to the sample to neutralize charge build up on the sample surface. Individual core levels were measured with a pass energy of 20 eV. The spectra were calibrated by setting the adventitious carbon 1 s peak to 284.8 eV. The background correction, calibration and peak fitting were done using ESCApe software.

Results and discussion

Initial nanocrystal characterisations

The $CsPbBr_3$ NC systems investigated in this study were produced following the room-temperature polar solvent-free synthesis route pioneered in our previous work.[38] A solution of Cs_2CO_3 in octanoic acid (OctA) is added to a solution containing $PbBr_2$, trioctylphosphine oxide (TOPO) and octylphosphonic acid (OPA) in toluene. The concentration of OPA utilised was shown to control the growth rate of the $CsPbBr_3$ NC in the subsequent reaction, whereas the addition of the bulky ligand didodecyldimethylammonium bromide (DDAB) quenches the NC growth. Hence, by varying the concentration of OPA and the duration of the reaction, the size of the produced NCs can be controlled. This method was used to produce 7 $CsPbBr_3$ NC samples (see Table 1 for synthesis parameters and sample naming). The nanocrystals were isolated via centrifugation in ethyl acetate and methyl acetate to produce a colloidal NC dispersion. A full discussion of the synthesis method can be seen in the previous work.

To confirm the production of the various NCs sizes, the colloidal solutions were examined via small angle x-ray scattering (SAXS), tunnelling electron microscope (TEM) imaging, and photoluminescence (PL) measurements. The SAXS analysis confirmed a range of mean particle diameters from 6.4 to 12.8 nm (Table 1; Figure 1) The NCs demonstrate relatively narrow Gaussian particle size distributions (FWHMs of 2-4 nm) that increase with particle size. The fitting of the SAXS curves can be seen in Figure S1. Figure 1 also shows TEM imaging of each NC sample (see Figure S2 for full images), corroborating a truncated octahedron morphology, observed previously in $CsPbBr_3$ NCs synthesized at an elevated temperature with phosphonic acids.[38,39]

The NC colloids demonstrated PL peak wavelengths that increased (red shifted) with particle size (Table 1; Figure S3), coherent with stronger quantum confinement as particle sizes approach and reduce below the exciton Bohr diameter of $CsPbBr_3$ (7 nm).[38] The quantum confinement phenomena are also responsible for the high PLQY values which range between 84 – 90 % (Figure S3).

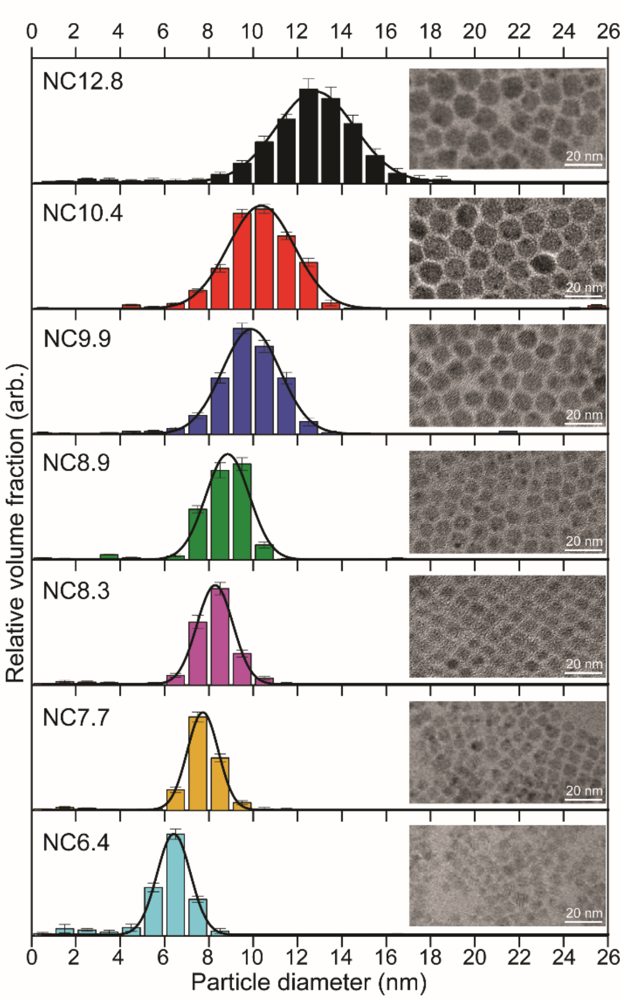

Figure 1: Particle diameter histograms from SAXS analysis of each $CsPbBr_3$ NC sample alongside TEM images.

To analyse the NCs with XRD and SSNMR, NC powders were produced by drying the colloids in air for 15 mins. TEM of the NC powders re-dispersed in heptane was used to confirm that particle size and/or morphology was not affected by this drying process (Figure S4). A bulk $CsPbBr_3$ powder was also produced for comparison with the NC samples. These powders were first observed with powder XRD, as shown in Figure 2. After Rietveld refinement the bulk sample was revealed to be 94% $CsPbBr_3$ with an orthorhombic *Pnma* space group, as expected from $CsPbBr_3$ crystals at room temperature, with the remainder made up of impurity phases.[40] Scherrer analysis of the bulk XRD pattern gives a mean crystallite size of 270 nm. The XRD patterns of the $CsPbBr_3$ NCs demonstrates broadened reflections coherent with nano-sized particles. The patterns are well fitted with a cubic *Pm-3m* space group, however some distinctive *Pnma* reflections ((102), (131) and (221) at 24.2°, 27.4° and 28.6° respectively) are just visible, suggesting at least

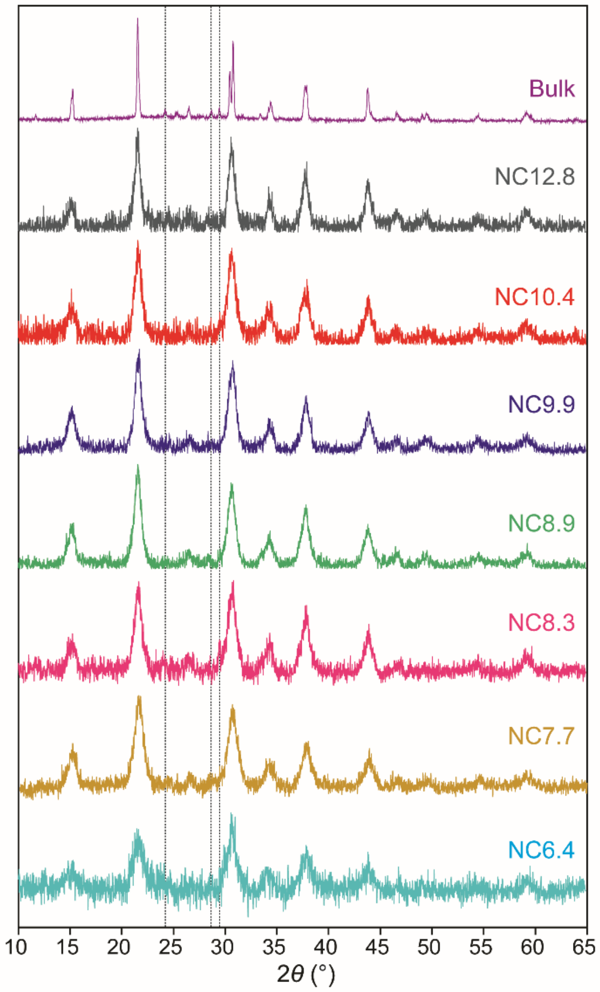

Figure 2: The powder XRD patterns of bulk $CsPbBr_3$ and the variable sized $CsPbBr_3$ NCs. Dashed lines mark characteristic orthorhombic *Pnma* reflections (102), (131) and (221).

some orthorhombic phases are present. Unfortunately, due to the nano-size broadening of the reflections, it is too difficult to give an accurate ratio of the phases. This is not unexpected, as the crystal phase of $CsPbBr_3$ NCs is still a matter of investigation.[41] Many have reported cubic $CsPbBr_3$ NCs from XRD results, whereas others have reported orthorhombic-structures, including Cottingham and Brutchey who utilised high-resolution synchrotron x-ray PDF analyses on 6.5 and 12.5 nm NCs.[41] Brennan et al. went further by investigating individual CsPbBr3 nanocrystals (10 nm diameter) with high resolution TEM, reporting a majority cubic/minority orthorhombic phase.[42]

Multinuclear solid state NMR

The ^{133}Cs NMR spectra for each of the NC powders are presented in Figure 3(a). The spectra of the nanocrystal samples are dominated by an asymmetric line shape, between 125 to 75 ppm, which has broad shoulders towards lower frequencies, indicating the presence of multiple overlapping ^{133}Cs environments. Similar asymmetric line shapes have been previously observed in the ^{133}Cs NMR of $CsPbBr_3$ NCs,[20,22,27,33] and in the SSNMR of various other nanoparticle systems.[43–46] Hence, these additional environments are presumed to be directly related to the nano-sized nature of the particles. Alternatively, the multiphase nature of the $CsPbBr_3$ NCs (*Pnma* and *Pm-3m*) could have resulted in multiple resonances. To disprove this possibility, variable temperature ^{133}Cs NMR was performed on bulk $CsPbBr_3$ (Figure S5) over the three structural phase regions of $CsPbBr_3$ (*Pnma* - 88°C – *P4/mbm* - 130°C – *Pm-3m*).[47] No sharp change in chemical shift could be seen at the phase transitions, and therefore it is assumed that the chemical shift difference between the orthorhombic and cubic phases is minimal. This finding is corroborated by previous studies which observed no difference in the ^{133}Cs chemical shift of $CsPbBr_3$ NCs with varying orthorhombic:cubic phase ratios.[27]

The NCs asymmetric ^{133}Cs line shapes are likely most accurately described by a continuous distribution of resonances, but for simulation and modelling purposes they have been fitted with the minimum required number of Gaussian resonances. Figure 3(a) shows how each of the dominant line shapes can be deconvoluted into 2-4 ^{133}Cs Gaussian resonances. The NMR parameters and relative integrals (i.e. percentage of Cs atoms in each environment) of the deconvolutions are given in Table 2. The majority of the NC samples' deconvoluted spectra present with 3 resonances around 116, 108 and 95 ppm, which get broader with lower frequency. Environments closer to the NC surface will give broadened resonances and altered chemical shift averages due to a greater distribution of local environments as a result of: distorted crystal structures due to the lattice truncation, higher vacancy concentrations near the surface, ligand bonding, etc. Hence, these 3 resonances are hypothesised to represent different layers within the NC structure which experience different amounts of distortion resulting from their immediacy to the NC surface.

Despite the predicted loss of crystalline symmetry in the system, no distinctive quadrupolar features are observed due to the very low ^{133}Cs quadrupolar moment ($Q = 0.343\ fm^2$).[45] The asymmetric line-shapes observed could alternatively be fit by a Gaussian distribution of quadrupolar resonances with varying quadrupolar coupling constants (C_Q), as shown in Figure S6. However these fits relied on an average C_Q of > 5 MHz, whereas the maximum reported ^{133}Cs C_Q from asymmetric crystalline environments is < 0.5 MHz.[48,49] Hence, such fits are not thought to represent reality and the ^{133}Cs quadrupolar interaction has been treated as negligible from here on.

Each of the NC samples also contains an additional resonance at 163 ppm. This resonance has previously been assigned as Cs environments which are interacting with ligands on the NC surface, which causes the large shift to higher frequency.[21]

The multiple Cs environments in the nanocrystals represented by the ^{133}Cs resonances were modelled under the assumption of a simplified spherical $CsPbBr_3$ NC (Figure 3(b)). The determined relative integrals of each of the resonances can be used to calculate volume ratios, and hence rough radial boundaries, of the proposed spherical model layers, by utilising several assumptions to allow a simple geometric calculation (see Supplementary Information for more details). The volume ratios and radial boundaries of the proposed layers can be seen in Table S1. The inner-most core layer is represented by the

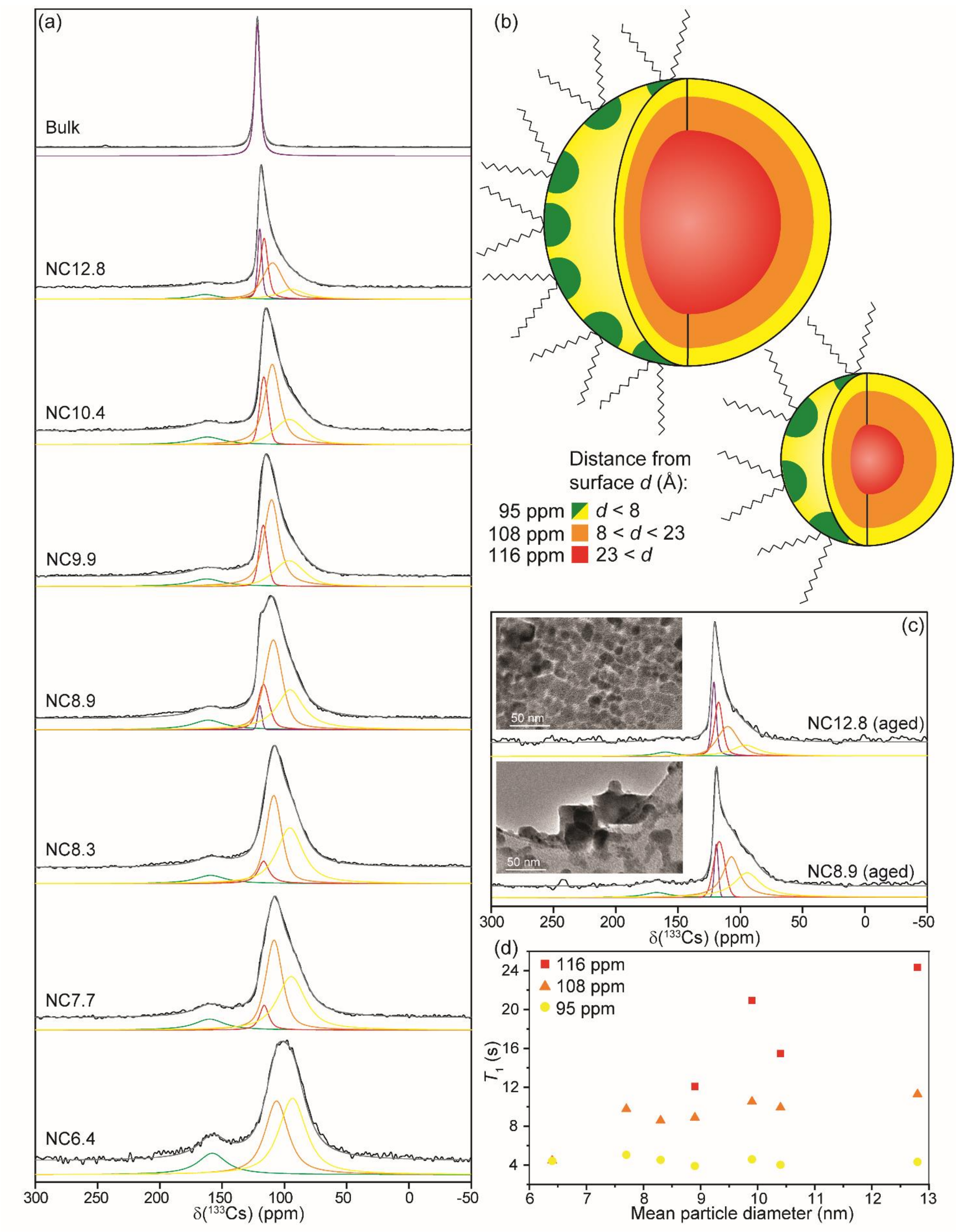

Figure 3: (a) The ^{133}Cs MAS NMR data of the bulk $CsPbBr_3$ and the variable sized $CsPbBr_3$ NCs with experimental spectra in black, simulated spectra in grey and colour coded (see (b)) deconvoluted components. (b) A schematic of two different sized NCs detailing the different nanoparticle layers via colours. (c) The ^{133}Cs MAS NMR data of NC12.8 and NC8.9 that have been aged under ambient conditions for 6 months with experimental spectra in black, simulated spectra in grey and colour coded deconvoluted components. TEM images of areas with particle agglomeration are inset. (d) A colour coded plot of the relaxation times T_1 of each NC layer against mean particle diameter.

Table 2. The ^{133}Cs NMR line shape deconvolution parameters and relaxation times T_1 with site assignments.

Sample name	Assignment	$\delta_{iso}(^{133}Cs)$ *(ppm)*	FWHM *(kHz)*	Relaxation T_1 *(s)*	Relative integrals *(%)*
Bulk [a]	Bulk	121.4 ± 0.3	0.39 ± 0.05	200 ± 10	100
NC12.8	Ligand adjacent	163 ± 1	1.9 ± 0.2	-	7
	Bulk	119.5 ± 0.2	0.32 ± 0.04	33 ± 2	15
	Nanocrystal layers	116.0 ± 0.9	0.56 ± 0.07	24 ± 1	24
		109 ± 1	1.5 ± 0.2	11.3 ± 0.6	38
		94 ± 2	2.0 ± 0.2	4.3 ± 0.4	16
NC10.4	Ligand adjacent	162 ± 2	2.4 ± 0.3	0.01 ± 0.01	10
	Nanocrystal layers	116.5 ± 0.5	0.63 ± 0.08	15.4 ± 0.7	17
		109.7 ± 0.9	1.1 ± 0.1	9.9 ± 0.2	47
		96 ± 2	2.2 ± 0.3	4.0 ± 0.3	26
NC9.9	Ligand adjacent	163 ± 2	2.4 ± 0.3	-	9
	Nanocrystal layers	117.1 ± 0.5	0.63 ± 0.08	20.9 ± 0.9	16
		110.4 ± 0.9	1.1 ± 0.1	10.6 ± 0.3	49
		96 ± 2	2.2 ± 0.3	4.6 ± 0.3	26
NC8.9	Ligand adjacent	161 ± 2	2.4 ± 0.3	-	9
	Bulk	119.5 ± 0.3	0.32 ± 0.04	36 ± 6	2
	Nanocrystal layers	116.4 ± 0.8	0.8 ± 0.1	12 ± 2	14
		109 ± 1	1.3 ± 0.2	8.9 ± 0.2	42
		95 ± 2	2.0 ± 0.3	3.9 ± 0.2	33
NC8.3	Ligand adjacent	159 ± 2	2.3 ± 0.3	0.02 ± 0.02	8
	Nanocrystal layers	116.5 ± 0.5	0.8 ± 0.1	-	8
		108 ± 1	1.2 ± 0.2	8.6 ± 0.2	39
		95 ± 2	1.9 ± 0.2	4.5 ± 0.2	45
NC7.7	Ligand adjacent	160 ± 2	2.3 ± 0.3	0.04 ± 0.04	10
	Nanocrystal layers	116.2 ± 0.7	0.7 ± 0.1	-	7
		108.3 ± 0.9	1.3 ± 0.1	9.8 ± 0.2	41
		95 ± 2	2.1 ± 0.3	5.0 ± 0.4	42
NC6.4	Ligand adjacent	158 ± 2	2.2 ± 0.3	-	15
	Nanocrystal layers	106 ± 1	1.6 ± 0.2	4.5 ± 0.4	38
		93 ± 2	2.0 ± 0.3	4.4 ± 0.3	47

- missing T_1 values are from smaller resonances that could not be accurately measured.

[a] Crystallite size of 0.27 μm determined by Scherrer analysis of XRD pattern

narrower resonance at 116 ppm, which can be modelled as including all Cs environments greater than ~23 Å from the surface. The second boundary is calculated as ~8 Å from the surface, with any Cs environments in this middle layer represented by the resonance at 108 ppm. The layer closest to the surface was determined using the relative integrals of both the "surface-adjacent" resonances at 95 ppm and the "ligand-adjacent" resonance at 163 ppm, giving a layer containing all Cs within ~8 Å from the NC surface. The Cs-Cs distance in $CsPbBr_3$ is 5.9 Å, therefore this layer includes the first closest Cs atoms to the surface. The spherical layer radii determined here were constrained across the suite of NC samples, but due to the assumptions made in the calculations they should be treated as estimates. However, the model is still instructive in visualising the nano-size induced radially increasing distortion in the NC structure and how that is represented in the NMR. The large concentrations of the distorted Cs environments detected in each NC sample by ^{133}Cs NMR, may help to explain the difficulty in determining the structural phase of $CsPbBr_3$ NCs seen in the literature.

Bulk $CsPbBr_3$ (Figure 3(a)) presents with a singular narrow ^{133}Cs NMR resonance at 121 ppm, which is in agreement with previous ^{133}Cs NMR of bulk (*Pnma*) $CsPbBr_3$ crystals.[26,30] This sharp resonance is also seen in samples NC12.8 and NC8.9. The presence of this component in two differently sized particle samples, but not in the other larger NCs, suggests this is the result of the anomalous formation of some larger particles in these two samples. After aging of the NC powders for 6 months, this resonance was found to increase in NC12.8 and NC8.9, as shown in Figure 3(c). This resonance also appeared in the aged versions of the other NCs (Figure S7). The TEM of these aged samples (Figure 3(c) inset and Figure S8) reveals that a small portion of the NCs have agglomerated into larger, often cuboid, crystals, demonstrating that agglomeration of the NCs occurs over time even when stored in solid form. The TEM of the aged samples helps to confirm the assignment of the 120 ppm resonance as anomalous agglomerated bulk $CsPbBr_3$, and hence this resonance was left out of the modelling of the NCs. A small impurity (< 1%) of Cs_4PbBr_6 could also be seen at 244 ppm in the ^{133}Cs NMR of some of the aged NCs (Figure S7), however the majority of the NCs were not chemically altered. The pressures and temperatures of MAS NMR may have contributed to the agglomeration, although these effects are fairly small (~10°C heating at 24 KHz). To eliminate this possibility, ^{133}Cs NMR was performed on a $CsPbBr_3$ NC sample after exaggerated periods of MAS spinning, with no effect observed (Figure S9).

Further information can be gained from the ^{133}Cs data by measuring the spin-lattice relaxation of each ^{133}Cs environment, which is sensitive to structural changes as well as motional dynamics. Table 2 details the characteristic spin-lattice relaxation time T_1 for each observed component in the ^{133}Cs spectra. The bulk $CsPbBr_3$ sample gives a long T_1 of 200 s, whereas the $CsPbBr_3$ NCs demonstrate much lower T_1 values of 4-24 s. Clearly, reduction to NC dimensions has a strong effect on the spin-lattice relaxation of the system, as demonstrated previously in $CsPbBr_3$[20] and other non-metallic systems.[46,50,51]

The T_1 values are shown to differentiate between the different NC layers, with the surface adjacent layer (95 ppm) and the middle layer (108 ppm) demonstrating T_1 values of around 9 and 4 s, respectively. These values are fairly consistent over the NC samples, as shown in Figure 3(d). The core layer (116 ppm) of the NC samples gives less consistent values, although for the larger NCs it is clearly a slower relaxing component. The variance in this value is not surprising considering the difficulties in measuring the relaxation of a smaller deconvoluted component of a larger line shape (values for NC6.4 and NC7.7 could not be achieved for this reason). However, the differentiable spin-lattice relaxation constants for different parts of the line shape lends support for the deconvolutions of the ^{133}Cs data and the layer model of the NC that was deduced from them. The increase in the relaxation rate for environments closer to the surface is explained by the larger distribution of local magnetic environments, which allows for more efficient spin-lattice relaxation.[46] The 163 ppm ^{133}Cs environment demonstrates relaxation that is 100 times as fast as the other environments. This corroborates the ligand-adjacent assignment of this resonance, as the highly mobile ligands will allow very fast relaxation.

Motional dynamics within the particle are also likely to play a role in the spin-lattice relaxation of the ^{133}Cs nuclei. Variable temperature T_1 measurements on $CsPbBr_3$ (Figure S5), suggests that ^{133}Cs in $CsPbBr_3$ are in the "slow-timescale regime" where faster motion results in faster spin-lattice relaxation.[20,52] The NC structural lattice is likely to allow more motion due to the lack of long range order and the presence of vacancies, which will contribute to the faster relaxation.[46] Dynamics may explain the faster T_1 values measured for the resonances of the larger agglomerated particles in NC12.8 and NC8.9. Despite having a similar ^{133}Cs line shape to microcrystalline $CsPbBr_3$, and hence being assigned as "bulk" $CsPbBr_3$, these environments have T_1 values of just over 30 s, much faster than the relaxation measured in the bulk $CsPbBr_3$ sample (200 s). Perhaps these particles still contain enough structural defects to effect the more sensitive spin-lattice relaxation.

Sample NC8.3 was chosen as a representative sample to be studied further with SSNMR. The ^{207}Pb NMR spectrum is shown in comparison with bulk $CsPbBr_3$ in Figure 4(a). The larger particles in the bulk sample demonstrate a multiplet pattern corresponding to scalar coupling between the ^{207}Pb (spin $I = 1/2$) metal centre and the six $^{79/81}$Br (spin $I = 3/2$) nuclei it is bonded to.[20,23,30] In contrast the NC ^{207}Pb spectrum shows a singular Gaussian resonance. This is due to chemical shift broadening of the individual spikelets in the scalar coupling pattern and/or faster relaxation of the $^{79/81}$Br nuclei which can effectively "self-decouple" the scalar coupling. Faster halide relaxation times in NC $CsPbX_3$ materials has been reported previously and was hypothesized to be the result of structural defects.[53] Both explanations corroborate the effects seen in the ^{133}Cs NMR of the $CsPbBr_3$ NCs.

To study the ligands present on the surface of the $CsPbBr_3$ NCs, sample NC8.3 was analysed with ^{13}C and ^{31}P NMR. Figure 4(b) shows the ^{13}C NMR spectrum of NC8.3 in comparison to the spectrum of pure DDAB powder. The ^{13}C data confirms the presence of DDA$^+$ in the NC sample, with the distinctive N**C**H_2/N**C**H_3 resonances observed at around 62/55 ppm. The ~ 6 ppm shift difference for the N**C**H_3 resonance between the spectra of NC8.3 and pure DDAB is due to the bonding of the DDAB N$^+$ to the NC surface where the steric didodecycl chains are likely to be orientated away from the surface leaving the methyl groups to be distorted. The ^{13}C NMR spectrum also determines that OctA has not remained on the NC surface, as the distinctive **C**OOH resonance (178 ppm) is not observed. The ^{31}P NMR spectra (Figure 4(c)) detected a small resonance at 25 ppm over a long acquisition time (1776 transients with a 180 s recycle delay). Brown *et al.* previously investigated $CsPbBr_3$ NCs with OPA ligands and assigned this resonance as mono-ionic OPA ligands which have bound to the nanocrystal surface via the P-O$^-$ functional group.[15] By measuring the integral of this resonance and comparing it to the integral of the ^{31}P resonance of a known sample (ammonium dihydrogen phosphate), the ^{31}P concentration can be determined which correlates to a very small OPA ligand weight percentage of 0.03 %. By assuming that the rest of the sample mass is made up of $CsPbBr_3$ NCs with a 8.3 nm diameter, we can estimate the OPA:NC ratio as less than 1 ligand per particle. Our previous work detailed the importance of the OPA ligand in controlling the NC growth,[38] however this result demonstrates that the more thorough washing routine employed in this synthesis (compared to Brown *et al.*[15]) must remove the majority of the phosphonic acid. TOPO, which as a free ligand presents with a resonance at 48 ppm (Figure S10), was not observed in the ^{31}P NMR spectrum.

A ^{133}Cs-^{1}H HETCOR NMR experiment was also performed on sample NC8.3, which is shown in Figure 4(d). The CP HETCOR sequence transfers polarisation from ^{1}H nuclei to ^{133}Cs nuclei, producing a 2D spectrum whose resonances represent correlations between spatially close H and Cs environments.

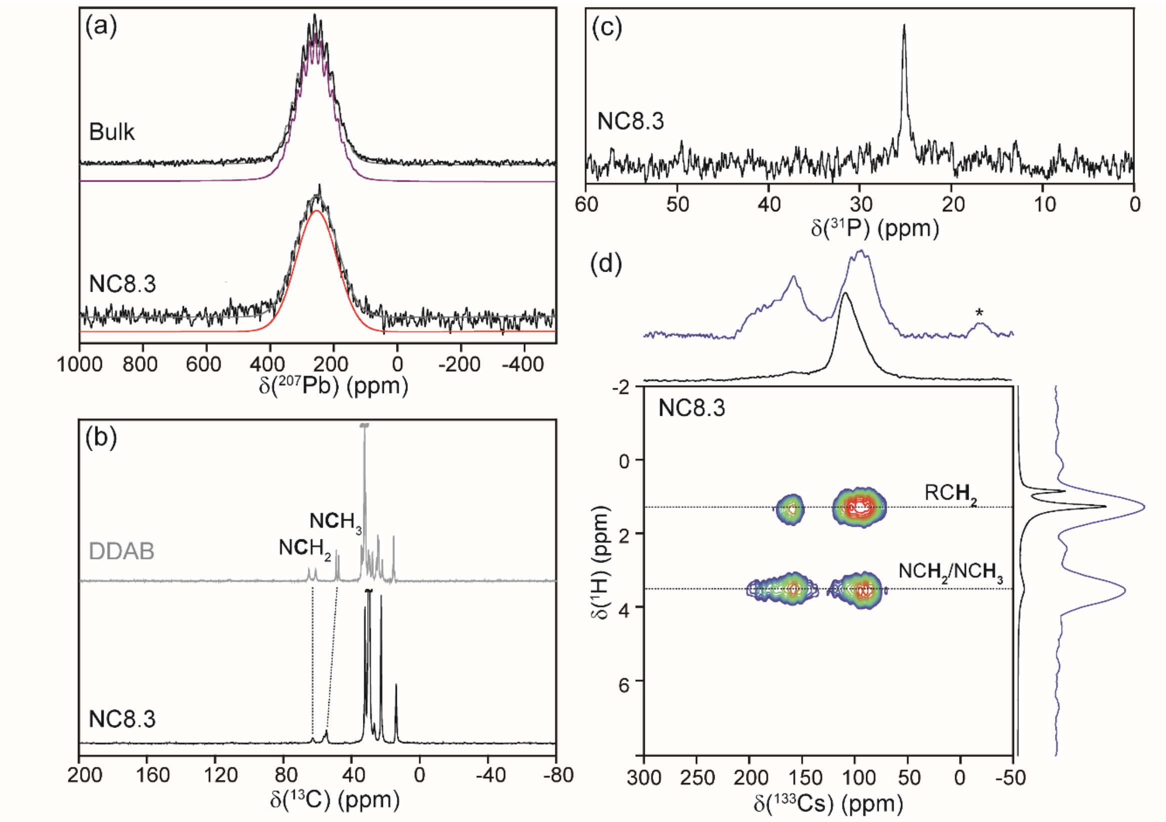

Figure 4: (a) The 207Pb MAS data of bulk CsPbBr3 and CsPbBr3 NC8.3 with experimental spectra in black, simulated spectra in grey and coloured deconvoluted components. (b) The 13C CPMAS spectrum of pure DDAB powder and CsPbBr3 NC8.3, where the nitrogen adjacent carbons have been marked. (c) The 31P MAS spectrum of CsPbBr3 NC8.3. (d) The 133Cs-1H 2D CPHETCOR of CsPbBr3 NC8.3, flanked by HETCOR projections in blue and 1D one-pulse spectra in black.

Chen *et al.* previously utilised the same experiment to confirm a correlation between a ~170 ppm ^{133}Cs resonance and the ^{1}H resonances of organic ligands for $CsPbBr_3$ quantum dots.[21]

In Figure 3(c), the ^{1}H spectrum is split into two DDA^{+} resonances: the nitrogen adjacent N**C**$\mathbf{H_2}$/N**C**$\mathbf{H_3}$ sites centred at 3.5 ppm; and the alkyl chain R**C**$\mathbf{H_2}$ sites centred at 1.2 ppm. These assignments are corroborated by the integral ratios of the analogous resonances (NC$\mathbf{H}_{2,3}$:RC$\mathbf{H_2}$ of 1:4) in the 1D ^{1}H NMR spectrum, which is shown alongside the ^{1}H projection in Figure 4(d). The larger relative increase in the NC$\mathbf{H_2}$/NC$\mathbf{H_3}$ resonance observed in the ^{1}H projection, is due to the closer proximity of these sites to the Cs on the NC surface due to the bonding through the N^{+} atom. The 163 ppm ^{133}Cs resonance is correlated to both ^{1}H resonances, demonstrating a large relative increase in the ^{133}Cs projection; this provides further evidence that this resonance represents surface Cs sites which are directly adjacent to the ligands. Correlations can also be seen with the more dominant ^{133}Cs NC resonance, albeit centred at 95 ppm. The chemical shift position corroborates the assignment of the lower frequency "shoulder" ^{133}Cs resonance as being close to the NC surface. The relative integral of this resonance in the ^{133}Cs projection is reduced implying that these sites are further from the ligands than the 163 ppm Cs sites.

X-ray photoelectron spectroscopy

To further investigate the surface of these NCs, XPS was employed (Figure 5(a)). The surface of the NCs is shown to be Br rich with Br/Pb atomic ratios fluctuating between 3.3 and 3.8. Bodnarchuk *et al.* previously discussed how high halide/lead ratios imply $CsPbX_3$ NC lattices which are terminated by a CsX shell or an AX′ passivating layer, where AX′ represents an ionic halide containing ligand.[54] Hence, these results are coherent with the theory that DDA^{+}Br^{-} ligands are passivating Cs^{+}/Br^{-} vacancies on the NC surface, as represented in Figure 5(b).[38,55,56] Ravi *et al.* performed a more in-depth, variable photon energy XPS study of $CsPbBr_3$ NCs, which concluded that the NCs are CsBr terminated with Cs^{+} vacancies. Chen *at al.* also recently provided convincing evidence of CsBr terminated $CsPbBr_3$ NCs with ammonium groups passivating Cs^{+} vacancies, via modelling of ^{1}H[^{133}Cs] and ^{1}H(^{207}Pb) RESPDOR curves.[21]

The seemingly random Br/Pb atomic ratios across the particle size range, are likely a result of the varying OPA concentration and reaction duration during the particle growth stage of the synthesis. From NC8.3 to NC10.4 a general trend of increasing Br/Pb ratio can be seen. These four NCs utilised the same reaction duration, with a decreasing OPA concentration. Therefore, it can be hypothesized that the lower OPA availability results in a lower OPA ligand density binding to under coordinated Pb on the NC surface, speeding particle growth as intended, but also increasing the concentration of

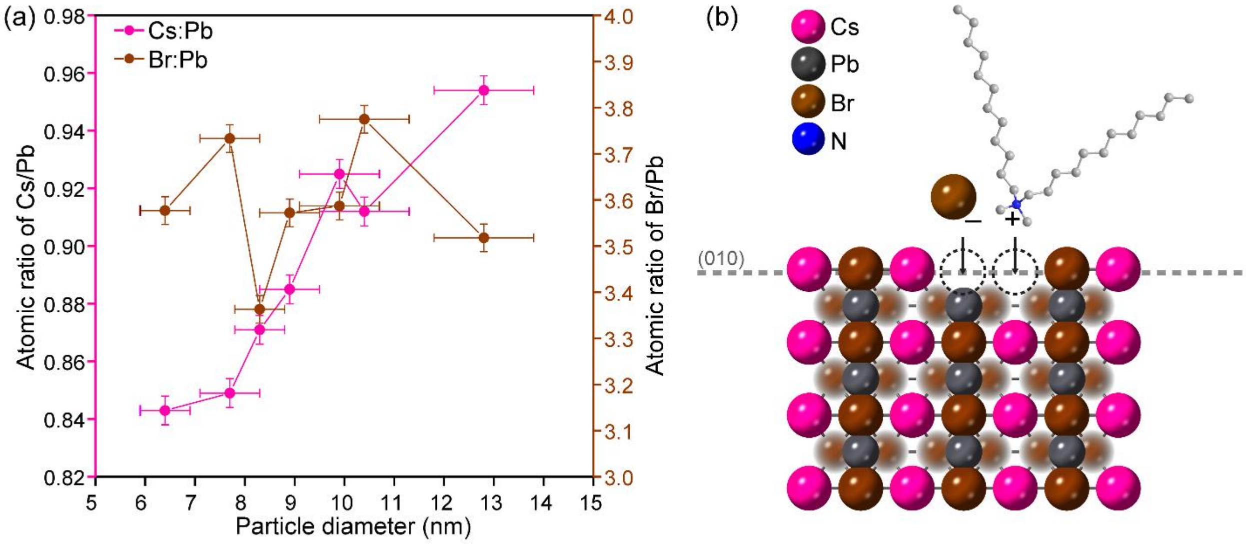

Figure 5: (a) The XPS determined surface atomic ratios of Cs/Pb and Br/Pb for the powder $CsPbBr_3$ NCs plotted against particle diameter. (b) Schematic representing the DDAB bonding at the NC surface

surface halide vacancies which can be passivated by DDAB. A higher density of DDAB ligands on the surface would then result in the higher Br/Pb ratios observed. The different reaction durations of the other three NCs would also alter the available DDAB binding sites and hence the Br/Pb ratio.

The Cs/Pb ratio decreases from 0.96 for NC12.8 to 0.84 for NC6.4. This suggests that the smaller NCs have a greater concentration of Cs^+ vacancies, which confirms the results of the ^{133}Cs NMR study. It is noted that NC10.4 can be seen to have a higher concentration of Cs vacancies than the smaller NC9.9, which is correlated by its faster ^{133}Cs spin-lattice relaxation, hinting that Cs vacancies play a strong role in the relaxation data. The XPS analysis also detected N at the NC surfaces (N/Pb = 0.3-0.5), which corroborates the presence of DDAB.

Conclusions

The thorough ^{133}Cs SSNMR study has revealed the radially increasing disorder present in $CsPbBr_3$ NCs, providing insight into the structural differences between different sized NCs. The study has also formalised ^{133}Cs NMR as a sensitive probe of NC particle size in the solid state, unlike conventional TEM/SAXS which require the NCs to be dispersed in solution as part of the sample preparation. Hence, this work has provided a foundation for further studies of Cs based perovskite NCs in optoelectronic device states, such as thin films/coatings. The combined SSNMR and XPS approach has determined DDAB to be the majority ligand present on the NC surface, passivating vacancies in the Cs-Br lattice truncation.

The $CsPbBr_3$ NCs are shown to be structurally stable in powder form under ambient conditions, albeit showing some particle agglomeration over a 6 month period, which could have important ramifications for their storage and transport in industrial applications.[13] These results are important to the further use of the facile room-temperature synthesis procedure implemented, which itself has great potential for further research into $CsPbX_3$ NC structure/ligand characterisation due to the size controlled NCs it produces. Post-synthetic ligand exchange would allow the direct effect of the ligands to be examined, without the interference of size effects. In depth characterisation of ligand-surface interactions, are highly important for current research in perovskite NCs, where surface-defect passivation can vastly improve optoelectronic performance while ligand properties can determine system qualities like stability and conductivity.[27,30,57–61]

Author Contributions

T.J.N.H.: writing – original draft, conceptualisation, investigation, funding acquisition; Y.F., A.A.M.B.: writing – review and editing, conceptualisation, investigation; S.H.P.: writing – review and editing, supervision; T.J.W.: writing – review and editing, supervision; funding acquisition.

Conflicts of interest

There are no conflicts to declare.

Acknowledgements

We thank the Singapore Ministry of Education, under the grant MOE2019-T2-2-032, and the Singapore National Research Foundation, under its Competitive Research Program (CRP Award No. NRF-CRP14-2014-03), for funding this research.

A.A.M.B. gratefully acknowledges the Tizard studentship from the Faculty of Engineering and Physical Sciences at the University of Southampton. We would like to acknowledge both the Center of High Field NMR Spectroscopy and Imaging and the Facility for Analysis, Characterization, Testing, and Simulation (FACTS) at Nanyang Technological University for the use of their facilities.

Notes and references

1 G. Li, J. Huang, H. Zhu, Y. Li, J. X. Tang and Y. Jiang, *Chemistry of Materials*, 2018, **30**, 6099–6107.
2 Q. Zhong, M. Cao, Y. Xu, P. Li, Y. Zhang, H. Hu, D. Yang, Y. Xu, L. Wang, Y. Li, X. Zhang and Q. Zhang, *Nano Letters*, 2019, **19**, 4151–4157.
3 J. Pan, Y. Shang, J. Yin, M. De Bastiani, W. Peng, I. Dursun, L. Sinatra, A. M. El-Zohry, M. N. Hedhili, A. H. Emwas, O. F. Mohammed, Z. Ning and O. M. Bakr, *Journal of the American Chemical Society*, 2018, **140**, 562–565.
4 N. Mondal, A. De and A. Samanta, *ACS Energy Letters*, 2019, **4**, 32–39.
5 F. Yan, S. T. Tan, X. Li and H. V. Demir, *Small*, 2019, **15**, 1902079.
6 X. Y. Chin, A. Perumal, A. Bruno, N. Yantara, S. A. Veldhuis, L. Martínez-Sarti, B. Chandran, V. Chirvony, A. S. Z. Lo, J. So, C. Soci, M. Grätzel, H. J. Bolink, N. Mathews and S. G. Mhaisalkar, *Energy and Environmental Science*, 2018, **11**, 1770–1778.
7 T. Leijtens, K. Bush, R. Cheacharoen, R. Beal, A. Bowring and M. D. McGehee, *Journal of Materials Chemistry A*, 2017, **5**, 11483–11500.
8 S. H. Turren-Cruz, A. Hagfeldt and M. Saliba, *Science*, 2018, **362**, 449–453.
9 M. Saliba, T. Matsui, J. Y. Seo, K. Domanski, J. P. Correa-Baena, M. K. Nazeeruddin, S. M. Zakeeruddin, W. Tress, A. Abate, A. Hagfeldt and M. Grätzel, *Energy and Environmental Science*, 2016, **9**, 1989–1997.
10 Q. A. Akkerman, G. Rainò, M. V. Kovalenko and L. Manna, *Nature Materials*, 2018, **17**, 394.
11 L. Protesescu, S. Yakunin, M. I. Bodnarchuk, F. Krieg, R. Caputo, C. H. Hendon, R. X. Yang, A. Walsh and M. V. Kovalenko, *Nano Lett.*, 2015, **15**, 3692–3696.
12 A. A. M. Brown, P. Vashishtha, T. J. N. Hooper, Y. F. Ng, G. V. Nutan, Y. Fang, D. Giovanni, J. N. Tey, L. Jiang, B. Damodaran, T. C. Sum, S. H. Pu, S. G. Mhaisalkar and N. Mathews, *Chem. Mater.*, 2021, **33**, 2387–2397.
13 A. A. M. Brown, B. Damodaran, L. Jiang, J. N. Tey, S. H. Pu, N. Mathews and S. G. Mhaisalkar, *Advanced Energy Materials*, 2020, **10**, 2001349.
14 L. Piveteau, V. Morad and M. V. Kovalenko, *J. Am. Chem. Soc.*, 2020, **142**, 19413–19437.
15 A. A. M. Brown, T. J. N. Hooper, S. A. Veldhuis, X. Y. Chin, A. Bruno, P. Vashishtha, J. N. Tey, L. Jiang, B. Damodaran, S. H. Pu, S. G. Mhaisalkar and N. Mathews, *Nanoscale*, 2019, **11**, 12370–12380.
16 R. Begum, X. Y. Chin, B. Damodaran, T. J. N. Hooper, S. Mhaisalkar and N. Mathews, *ACS Appl. Nano Mater.*, 2020, **3**, 1766–1774.
17 V. K. Ravi, P. K. Santra, N. Joshi, J. Chugh, S. K. Singh, H. Rensmo, P. Ghosh and A. Nag, *The Journal of Physical Chemistry Letters*, 2017, **8**, 4988–4994.
18 D. Quarta, M. Imran, A.-L. Capodilupo, U. Petralanda, B. van Beek, F. De Angelis, L. Manna, I. Infante, L. De Trizio and C. Giansante, *The Journal of Physical Chemistry Letters*, 2019, 3715–3726.
19 P. Vashishtha, T. J. N. Hooper, Y. Fang, D. Kathleen, D. Giovanni, M. Klein, T. Chien Sum, S. G. Mhaisalkar, N. Mathews and T. White, *Nanoscale*, 2021, **13**, 59–65.
20 P. Vashishtha, S. A. Veldhuis, S. S. H. Dintakurti, N. L. Kelly, B. E. Griffith, A. A. M. Brown, M. S. Ansari, A. Bruno, N. Mathews, Y. Fang, T. White, S. G. Mhaisalkar and J. V. Hanna, *J. Mater. Chem. C*, 2020, **8**, 11805–11821.
21 Y. Chen, S. R. Smock, A. H. Flintgruber, F. A. Perras, R. L. Brutchey and A. J. Rossini, *J. Am. Chem. Soc.*, , DOI:10.1021/jacs.9b13396.
22 J. Shamsi, D. J. Kubicki, M. Anaya, Y. Liu, K. Ji, K. Frohna, C. P. Grey, R. H. Friend and S. D. Stranks, *ACS Energy Letters*, , DOI:10.1021/acsenergylett.0c00935.
23 M. Aebli, L. Piveteau, O. Nazarenko, B. M. Benin, F. Krieg, R. Verel and M. V. Kovalenko, *Scientific Reports*, 2020, **10**, 8229.
24 A. Ray, D. Maggioni, D. Baranov, Z. Dang, M. Prato, Q. A. Akkerman, L. Goldoni, E. Caneva, L. Manna and A. L. Abdelhady, *Chemistry of Materials*, 2019, **31**, 7761–7769.
25 C. Roiland, G. Trippé-Allard, K. Jemli, B. Alonso, J.-C. Ameline, R. Gautier, T. Bataille, L. Le Pollès, E. Deleporte, J. Even and C. Katan, *Physical Chemistry Chemical Physics*, 2016, **18**, 27133–27142.
26 A. Karmakar, M. S. Dodd, X. Zhang, M. S. Oakley, M. Klobukowski and V. K. Michaelis, *Chem. Commun.*, 2019, **55**, 5079–5082.
27 P. Vashishtha, B. E. Griffith, A. A. M. Brown, T. J. N. Hooper, Y. Fang, M. S. Ansari, A. Bruno, S. H. Pu, S. G. Mhaisalkar, T. White and J. V. Hanna, *ACS Appl. Electron. Mater.*, 2020, **2**, 4002–4011.
28 D. J. Kubicki, D. Prochowicz, A. Hofstetter, S. M. Zakeeruddin, M. Grätzel and L. Emsley, *Journal of the American Chemical Society*, 2017, **139**, 14173–14180.
29 D. J. Kubicki, D. Prochowicz, A. Pinon, G. Stevanato, A. Hofstetter, S. M. Zakeeruddin, M. Grätzel and L. Emsley, *J. Mater. Chem. A*, 2019, **7**, 2326–2333.
30 A. Kanwat, N. Yantara, Y. F. Ng, T. J. N. Hooper, P. J. S. Rana, B. Febriansyah, P. C. Harikesh, T. Salim, P. Vashishtha, S. G. Mhaisalkar and N. Mathews, *ACS Energy Lett.*, 2020, **5**, 1804–1813.
31 D. J. Kubicki, M. Saski, S. MacPherson, K. Gałkowski, J. Lewiński, D. Prochowicz, J. J. Titman and S. D. Stranks, *Chem. Mater.*, 2020, **32**, 8129–8138.
32 A. Karmakar, A. Bhattacharya, G. M. Bernard, A. Mar and V. K. Michaelis, *ACS Materials Lett.*, 2021, 261–267.
33 L. Xie, P. Vashishtha, T. M. Koh, P. C. Harikesh, N. F. Jamaludin, A. Bruno, T. J. N. Hooper, J. Li, Y. F. Ng, S. G. Mhaisalkar and N. Mathews, *Advanced Materials*, 2020, **32**, 2003296.
34 L. Piveteau, T.-C. Ong, A. J. Rossini, L. Emsley, C. Copéret and M. V. Kovalenko, *J. Am. Chem. Soc.*, 2015, **137**, 13964–13971.
35 R. K. Harris, E. D. Becker, S. M. Cabral De Menezes, R. Goodfellow and P. Granger, *International Union of Pure and Applied Chemistry*, 2002, **1**, 43–64.
36 R. K. Harris, E. D. Becker, S. M. Cabral de Menezes, P. Granger, R. E. Hoffman and K. W. Zilm, *Pure and Applied Chemistry*, 2008, **80**, 59–84.
37 D. Massiot, F. Fayon, M. Capron, I. King, S. Le Calvé, B. Alonso, J.-O. Durand, B. Bujoli, Z. Gan and G. Hoatson, *Magnetic Resonance in Chemistry*, 2002, **40**, 70–76.
38 A. Brown, P. Vashishtha, T. Hooper, Y. F. Ng, G. Nutan, Y. Fang, D. Giovanni, J. N. Tey, L. Jiang, B. Damodaran, T. C. Sum, S. H. Pu, S. Mhaisalkar and N. Mathews, *Chemistry of Materials*.

39 B. Zhang, L. Goldoni, J. Zito, Z. Dang, G. Almeida, F. Zaccaria, J. de Wit, I. Infante, L. De Trizio and L. Manna, *Chem. Mater.*, 2019, **31**, 9140–9147.

40 S. Hirotsu, J. Harada, M. Iizumi and K. Gesi, *J. Phys. Soc. Jpn.*, 1974, **37**, 1393–1398.

41 P. Cottingham and R. L. Brutchey, *Chem. Commun.*, 2016, **52**, 5246–5249.

42 M. C. Brennan, M. Kuno and S. Rouvimov, *Inorg. Chem.*, 2019, **58**, 1555–1560.

43 S. Cadars, B. J. Smith, J. D. Epping, S. Acharya, N. Belman, Y. Golan and B. F. Chmelka, *Phys. Rev. Lett.*, 2009, **103**, 136802.

44 G. J. Rees, S. T. Orr, L. O. Barrett, J. M. Fisher, J. Houghton, G. H. Spikes, B. R. C. Theobald, D. Thompsett, M. E. Smith and J. V. Hanna, *Physical Chemistry Chemical Physics*, 2013, **15**, 17195.

45 Thomas J. N. Hooper, T. A. Partridge, G. J. Rees, D. S. Keeble, N. A. Powell, M. E. Smith, I. P. Mikheenko, L. E. Macaskie, P. T. Bishop and J. V. Hanna, *Phys. Chem. Chem. Phys.*, 2018, **20**, 26734–26743.

46 A. N. Thiessen, M. Ha, R. W. Hooper, H. Yu, A. O. Oliynyk, J. G. C. Veinot and V. K. Michaelis, *Chem. Mater.*, 2019, 11.

47 D. Yang and D. Huo, *J. Mater. Chem. C*, 2020, **8**, 6640–6653.

48 J. Skibsted, T. Vosegaard, H. Bildsøe and H. J. Jakobsen, *J. Phys. Chem.*, 1996, **100**, 14872–14881.

49 S. Mooibroek, R. E. Wasylishen, R. Dickson, G. Facey and B. A. Pettitt, *Journal of Magnetic Resonance (1969)*, 1986, **66**, 542–545.

50 T. Dey, P. Khuntia, A. V. Mahajan, N. Kumar and A. Sundaresan, 6.

51 J. W. Aptekar, M. C. Cassidy, A. C. Johnson, R. A. Barton, M. Lee, A. C. Ogier, C. Vo, M. N. Anahtar, Y. Ren, S. N. Bhatia, C. Ramanathan, D. G. Cory, A. L. Hill, R. W. Mair, M. S. Rosen, R. L. Walsworth and C. M. Marcus, 2009, **3**, 6.

52 J. L. Sudmeier, S. E. Anderson and J. S. Frye, *Concepts Magn. Reson.*, 1990, **2**, 197–212.

53 L. Piveteau, M. Aebli, N. Yazdani, M. Millen, L. Korosec, F. Krieg, B. M. Benin, V. Morad, C. Piveteau, T. Shiroka, A. Comas-Vives, C. Copéret, A. M. Lindenberg, V. Wood, R. Verel and M. V. Kovalenko, *ACS Cent. Sci.*, 2020, **6**, 1138–1149.

54 M. I. Bodnarchuk, S. C. Boehme, S. ten Brinck, C. Bernasconi, Y. Shynkarenko, F. Krieg, R. Widmer, B. Aeschlimann, D. Günther, M. V. Kovalenko and I. Infante, *ACS Energy Lett.*, 2019, **4**, 63–74.

55 Y. Shynkarenko, M. I. Bodnarchuk, C. Bernasconi, Y. Berezovska, V. Verteletskyi, S. T. Ochsenbein and M. V. Kovalenko, *ACS Energy Lett.*, 2019, **4**, 2703–2711.

56 Z. Zang and D. Yan, in *Perovskite Quantum Dots: Synthesis, Properties and Applications*, eds. Y. Zhou and Y. Wang, Springer, Singapore, 2020, pp. 51–106.

57 F. Li, Y. Liu, H. Wang, Q. Zhan, Q. Liu and Z. Xia, *Chem. Mater.*, 2018, **30**, 8546–8554.

58 Y. Liu, F. Li, Q. Liu and Z. Xia, *Chem. Mater.*, 2018, **30**, 6922–6929.

59 K. Hills-Kimball, H. Yang, T. Cai, J. Wang and O. Chen, *Advanced Science*, 2021, **8**, 2100214.

60 J. Xue, R. Wang and Y. Yang, *Nat Rev Mater*, 2020, **5**, 809–827.

61 J. Shamsi, A. S. Urban, M. Imran, L. De Trizio and L. Manna, *Chem. Rev.*, 2019, **119**, 3296–3348.